nature communications

Article

https://doi.org/10.1038/s41467-024-55074-4

Nondestructive halide exchange via S_N2-like mechanism for efficient blue perovskite light-emitting diodes

Received: 18 July 2024

Accepted: 29 November 2024

Published online: 05 December 2024

Check for updates

Kai Zhang[1,5], Yang Shen[1,2,5] ✉, Long-Xue Cao[2,5], Zhen-Huang Su[3], Xin-Mei Hu[2], Shi-Chi Feng[2], Bing-Feng Wang[4], Feng-Ming Xie[2], Hao-Ze Li[4], Xingyu Gao[3], Yan-Qing Li[4] ✉ & Jian-Xin Tang[1,2] ✉

Blue perovskite light-emitting diodes (PeLEDs) still remain poorly developed due to the big challenge of achieving high-quality mixed-halide perovskites with wide optical bandgaps. Halide exchange is an effective scheme to tune the emission color of PeLEDs, while making perovskites susceptible to high defect density due to solvent erosion. Herein, we propose a versatile strategy for nondestructive in-situ halide exchange to obtain high-quality blue perovskites with low trap density and tunable bandgaps through long alkyl chain chloride incorporated chloroform post-treatment. In comparison with conventional halide exchange method, the ionic exchange mechanism of the present strategy is similar to a bimolecular nucleophilic substitution process, which simultaneously modulates perovskite bandgaps and inhibits new halogen vacancy generation. Consequently, efficient PeLEDs across blue spectral regions are obtained, exhibiting external quantum efficiencies of 23.6% (sky-blue emission at 488 nm), 20.9% (pure-blue emission at 478 nm), and 15.0% (deep-blue emission at 468 nm), respectively.

Although blue perovskite light-emitting diodes (PeLEDs) have achieved impressive external quantum efficiencies (EQEs) over 20%, these state-of-the-art devices are still limited to sky-blue spectral range (>480 nm)[1–5]. Due to the demanding requirements to address crystal defect passivation and wide bandgap regulation simultaneously, obtaining blue perovskite emitters that comply with the standard of National Television System Committee (NTSC) remains a major challenge[6,7]. Constructing small-*n* (*n* represents the number of inorganic octahedron sheets) perovskite phases with strong quantum confinement by incorporating organic spacers can achieve blue-shifted emission and reduce defect density, which, however, enhances exciton-phonon coupling to cause severe non-radiative transitions[8,9]. In addition, the hindered charge transport, disordered phase distribution, and severe Auger recombination in reduced-dimensional perovskites also limit the application of size engineering in pure- and deep-blue PeLEDs[10,11]. Adjusting the halogen ion ratio in precursor allows for convenient achievement of wide bandgap, but the low solubility of chlorides results in poor quality of mixed-halide blue perovskite films[12,13]. Therefore, altering precursor composition to manipulate perovskite crystallization for blue emission is prone to induce detrimental phase segregation, high defect density, and low defect tolerance for blue perovskites[14].

Halide exchange strategy has been demonstrated to adjust halogen ion ratios in perovskites through proper solvent post-treatment without altering the precursor composition[6,15,16]. For example, Wang et al. reported a direct halide exchange method to achieve deep-blue

[1]Macao Institute of Materials Science and Engineering (MIMSE), Faculty of Innovation Engineering, Macau University of Science and Technology, Taipa, Macao, China. [2]Institute of Functional Nano & Soft Materials (FUNSOM), Jiangsu Key Laboratory for Carbon-Based Functional Materials & Devices, Soochow University, Suzhou, China. [3]Shanghai Synchrotron Radiation Facility, Zhangjiang Laboratory, Chinese Academy of Sciences, Shanghai, China. [4]School of Physics and Electronic Science, East China Normal University, Shanghai, China. [5]These authors contributed equally: Kai Zhang, Yang Shen, Long-Xue Cao.
✉e-mail: yangshen@suda.edu.cn; yqli@phy.ecnu.edu.cn; jxtang@must.edu.mo

PeLEDs with a maximum external quantum efficiency (EQE_{max}) of 4.6% by incorporating organic ammonium salt ligands[6]. This method simultaneously adjusted the bandgap of perovskite films and passivated defects. However, the selection of post-treatment solvents and Cl sources for halide exchange strategy presents a challenging trade-off[17]. Especially, as a prevailing post-treatment solvent[18,19], isopropanol (IPA) facilitates the dissolution of organic halide ammonium salts while unfortunately causes significant erosion of perovskite films, resulting in numerous pinholes and increased defect density[6,15]. This dilemma makes anti-solvents as promising candidate for new-generation halide exchange strategy. Although anti-solvents such as chloroform (CF) effectively avoid solvent erosion on perovskite films, their poor dissolving capacity results in a lack of suitable organic ammonium salts as Cl sources for halide exchange[16,17,20]. Inspired by enhancing the solubility of organic active materials for solar cells through constructing long alkyl chains[21,22], long alkyl chains halide ammonium salts, as Cl sources, may possess good solubility in anti-solvents, which provides an great opportunity for selective ion exchange in perovskite films.

Here, we present a nondestructive halide exchange strategy, as shown in Fig. 1a, consisting of three key components: First, inhibition of solvent erosion of perovskite films during anti-solvent post-treatment; Second, improved solubility of halide ammonium salts through long alkyl chains in the anti-solvent; Third, achieving tunable bandgap of perovskite films through in situ halide exchange with Br and Cl atoms. Specifically, we employ anti-solvent CF-based post-treatment combined with long alkyl chain butylammonium halide (BAX, X = Br, Cl) to generate tunable emission across the wide blue spectral range. In view of the negligible effect of pure CF on perovskite films, a S_N2-like mechanism is applied to describe the ion exchange process, where the Cl atom attacks the Pb atom accompanied by the desorption of Br

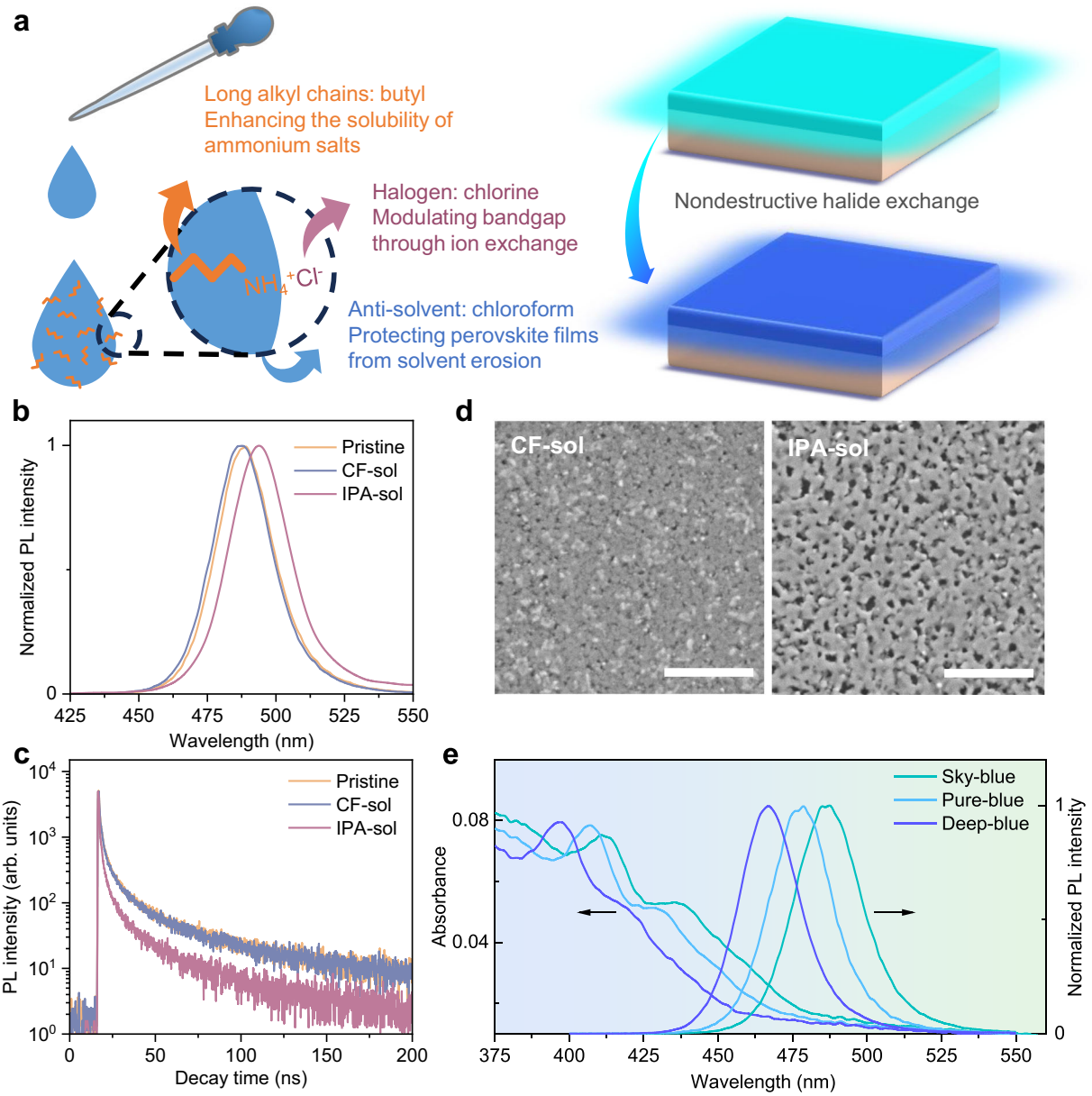

Fig. 1 | Nondestructive halide exchange strategy. a Schematic diagram of nondestructive halide exchange strategy. **b** PL spectra of pristine and solvent post-treated perovskite films. **c** TRPL spectra of pristine and solvent post-treated perovskite films. **d** Top-view SEM images of pristine and solvent post-treated perovskite films. Scale bars: 500 nm. **e** PL and absorption spectra of BAX-based CF post-processed $BABr_{0.7}Cl_{0.3}$, $BABr_{0.4}Cl_{0.6}$ and $BABr_{0.1}Cl_{0.9}$ films, which achieve sky-, pure-, and deep-blue emission, respectively.

atom from lattice. This mechanism differs significantly from the S_N1-like halide exchange mechanism for conventional IPA-based post-treatment, which generates halogen vacancies by perovskite dissolution and then induces vacancy filling with Cl atoms. Leveraging the S_N2-like mechanism, the newly developed halide exchange strategy avoids the formation of new halogen vacancies, resulting in spectrally tunable blue perovskite films with low defect density and high photoluminescence quantum yields (PLQYs). Consequently, efficient blue PeLEDs exhibit excellent EQE_{max} of 23.6%, 20.9%, and 15.0% with emission peaks at 488, 478, and 468 nm, respectively, which stands out from the state-of-the-art blue PeLEDs at the present stage.

Results

The effect of different solvents on halide exchange

As representative solvents, CF and IPA were utilized to first investigate their solvent erosion effects on the quasi two-dimensional (quasi-2D) $CsPb(Br/Cl)_3$ perovskite films during post-treatment. As expected, CF treatment exerted negligible impact on the photophysical property of perovskite films, as evidenced by both the photoluminescence (PL) and time-resolved photoluminescence (TRPL) spectra (Fig. 1b, c). In contrast, the IPA treated sample exhibits a red-shifted PL spectrum (498 nm), which can be attributed to the partially elimination of low-*n* phases due to the dissolution of organic ligand 4-fluorophenylethylammonium bromide (*p*-F-PEABr). TRPL decay profiles can be fitted by tri-exponential decay functions and all the parameters extracted by the fitted curves are summarized in Supplementary Table 1. This results in a significant increase in defect density and a greatly shortened average TRPL lifetime (τ_{avg}) to 9.26 ns as compared to the τ_{avg} (21.58 ns) in pristine film (Fig. 1b). The substantial variations in photophysical property are ascribed to the distinct solubility of perovskite precursor components in CF and IPA. Specifically, precursor components are almost insoluble in CF, which suppresses the solvent erosion and thus preserves the uniform and dense film morphology, as shown in Fig. 1d. By contrast, the excellent solubility of organic ligand and halide cesium precursors in IPA leads to rapid perovskite dissolution during post-treatment[23], which damages the perovskite crystal structure and results in increased film pinholes. Further evidence was provided by the energy-dispersive X-ray spectroscopy (EDS) analysis of the dissociated components from original perovskite films during treatment processes. As depicted in Supplementary Figs. 1 and 2, the EDS mapping pictures indicate that the IPA post-treatment apparently removes part Cs and halogen atoms from the sample, which directly causes the formation of large film pinholes and crystal defects. Conversely, barely no precursor elemental signals can be observed after CF post-treatment, demonstrating the protective effect of the anti-solvent on perovskite film. To examine the impact of different solvent post-treatment on the electroluminescence (EL) of perovskites, the corresponding PeLEDs with a structure of indium tin oxide (ITO)/PEDOT:PSS/perovskite/1,3,5-Tris(1-phenyl-1H-benzimidazol-2-yl)benzene (TPBi)/lithium fluoride (LiF)/aluminum (Al) were fabricated. The optimal ratio of the modifier ethanolamine (ETA) in PEDOT:PSS was first screened. By comparison, the device based on the PEDOT:PSS layer doped with ETA of 4 vol.‰ (denoted as ETA-4) exhibits the best performance, hence we selected ETA-4 as the hole transport layer for further investigation (Supplementary Figs. 3,4). Consistent with the PL results, the pristine device exhibits a sky-blue emission at 490 nm with an EQE_{max} of 13.53%, while the IPA-treated device shows a significantly lower EQE_{max} of 0.83% at 498 nm (Supplementary Fig. 5). This thirteen-fold efficiency loss can be attributed to trap-assisted nonradiative recombination and increased leakage current due to poor film quality. By contrast, the CF-treated device maintains a decent EQE_{max} of 13.15% at 490 nm, underscoring the importance of appropriate solvent selection in post-treatment. To induce effective halide exchange, it's necessary to guarantee a good solubility of halogen sources. Accordingly, we chose organic ammonium salts with long alkyl chains as the solute in CF. As verified in Supplementary Fig. 6, despite *p*-F-PEABr and BABr having similar molecular lengths, the noticeable solubility difference suggests that the solubility enhancement scheme by using long alkyl chains is equally applicable to organoammonium salts.

As expected, spin-coating BACl/BABr mixed solution (CF as solvent) onto the pristine perovskite film can effectively tune its PL spectrum from sky- to deep-blue region via in situ halide exchange. As displayed in Fig. 1e, PL measurements reveal that an increase in chloride ratio in the post-treatment solution contributes to enlarged optical bandgaps from 488 to 468 nm. The absorption spectra showcase a similar trend with distinctly blue-shifted absorption edges as the Br/Cl ratio decreases. Considering the poor solubility of spacer *p*-F-PEABr in CF, we speculate that the bandgap enlargement originates from the lower Br/Cl ratio in the treated perovskite films, rather than quasi-2D phase rearrangement. As confirmed in Supplementary Fig. 7 and Table 2, X-ray photoelectron spectroscopy (XPS) results present a clear negative correlation between the Br/Cl ratio and the bandgaps of post-treated perovskite films. X-ray diffraction (XRD) patterns reveal that the dominant XRD peak shifts to larger diffraction angles (Supplementary Fig. 8), suggesting the lattice shrinking with the substitution of smaller Cl for Br atoms[24]. To verify the unchanged quasi-2D phase arrangement, grazing-incidence wide-angle X-ray scattering (GIWAXS) measurements were utilized to examine the crystalline structure of the pristine and post-treated perovskite films. As shown in Supplementary Fig. 9, no signal from new small-*n* phases is observed in the post-treated films, which is consistent with the UV absorption results. Concluding from the above results, the proposed CF-based post-treatment can effectively modulate perovskite bandgaps via halide exchange and inhibit new defect generation in perovskite films.

Underlying mechanisms of halide exchange

To gain insights into the halide exchange mechanism, drawing from organic reaction mechanisms, we establish S_N2- and S_N1-like models to describe the ion migration pathways during CF and IPA post-treatment processes, respectively[25,26]. As depicted in Fig. 2a, the halide exchange proceeding in conventional IPA-based treatment involves two sequential steps, similar to the S_N1 nucleophilic substitution in organic reactions. First, the high solubility of halogens in IPA facilitates the spontaneous desorption of Br ions and hence generates vacancies (Step A). Subsequently, free Cl ions fill in these halogen vacancies through perovskite recrystallization, thus completing the halogen ion exchange process (Step B). It's worth noting that the halide dissociation in Step A has been verified, which is attributed to the IPA-induced erosion effect on perovskite films (Fig. 1d and Supplementary Fig. 2). This phenomenon results in severe fluorescence quenching as confirmed by the in-situ fluorescence monitoring during post-treatment (Fig. 2b). The initial stage (at 1 s) of IPA post-treatment shows a significant decrease in fluorescence intensity, which originates from the surge in newly formed halide vacancies[6]. Then, the IPA post-treated film gradually releases brighter and blue-shifted emission after 3 s on account of the halogen filling process as depicted in Step B (Fig. 2a). This phenomenon suggests that the filling of halide vacancies not only contributes to an increased bandgap by altering the Br/Cl ratio, but also suppresses the trap-mediated nonradiative recombination. However, the halogen filling effect fails to make up for the halogen loss induced by the IPA-based post-treatment, resulting in shortened TRPL lifetimes compared to that of pristine film (Supplementary Fig. 10). Thereby, IPA-based halide exchange strategy is expected to hold limited potential in producing high-performance mixed-halide blue perovskites and devices.

On the contrary, the negligible erosion effect of CF-based post-treatment on perovskite films prevents the emerge of new halide

https://doi.org/10.1038/s41467-024-55074-4

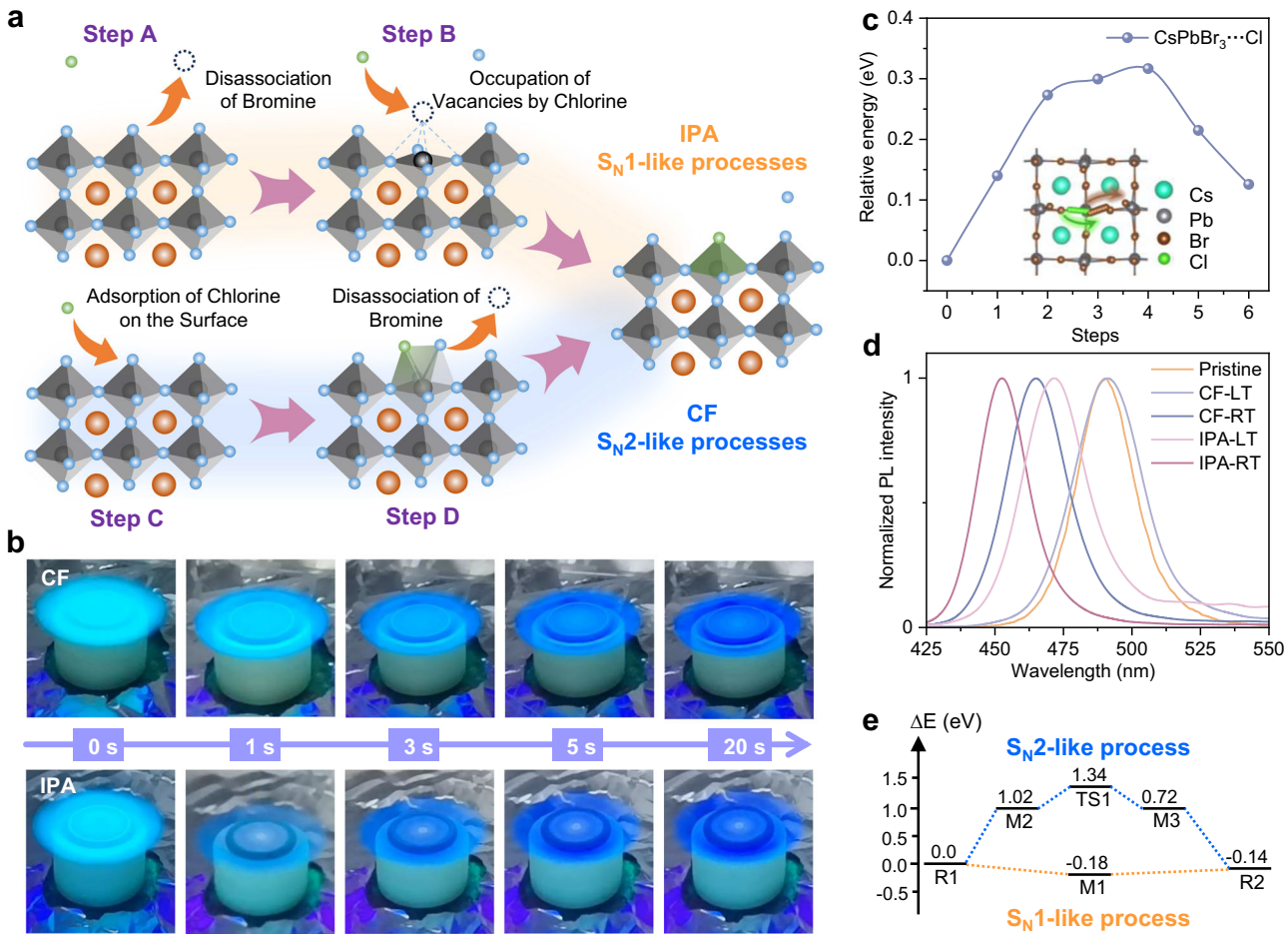

Fig. 2 | Underlying mechanism of halogen ion exchange. a Schematics of ion exchange reactions based on the S_N1-like mechanism (IPA post-treatment) and the S_N2-like mechanism (CF post-treatment). **b** Real-time fluorescence monitoring images during IPA and CF in-situ post-treatment. **c** Relative energy landscapes for ion migration pathway in S_N2-like halogen exchange process. The inset shows the theoretical models of the perovskite lattices during the exchange process. **d** Low-temperature (LT) and room-temperature (RT) post-treatment of PL spectra of CF and IPA solvents. **e** Potential energy profiles in halogen ion exchange pathways based on S_N1-like and S_N2-like mechanisms. (R1: reactants, $CsPbBr_3$ + Cl. R2: product, $CsPbBr_2Cl$ + Br. Intermediate for S_N1-like process: M1: surface defects of Br, $CsPbBr_2$-defect + Br + Cl. Intermediate for S_N2-like process: M2: Cl adsorbed in crystal surface, $CsPbBr_3$•••Cl; M3: Br adsorbed in crystal surface, $CsPbBr_2Cl$•••Br; TS1: transition states, $CsPbBr_2$•••Br•••Cl).

vacancies, fundamentally differentiating it from the ionic exchange mechanism in IPA treatment. As depicted in Fig. 2a, an S_N2-like mechanism is used to describe the halide exchange process for CF-based post-treatment. At the initial stage, Cl ions adsorb onto the lattice by attacking Pb atoms (Step C), then the local lattice distortion facilitates the exchange of halogen position. The ion migration pathway is simulated by using transition state theory (Fig. 2c), where molecular internal translation results in an intermediate structure with the coexistence of Br and Cl ions at the original lattice site. Finally, the desorption of Br atoms completes the halide exchange process (Step D), producing mixed-halide perovskite crystals with increased bandgaps. After the surface halogen ion exchange, locally inhomogeneous ion distribution drives the Cl ions to penetrate into perovskite crystals, while the inside Br ions spreads to the film surface. Consequently, this nondestructive halide exchange leads to uniform and blue-shifted fluorescence through the S_N2-like mechanism (Fig. 2b). Notably, the significant difference in fluorescence intensity between IPA and CF post-treated films as monitored at 1 s further corroborates the distinct ion behavior in these two mechanisms. Such discrepancy regarding halogen ionic behavior can be ascribed to the different driving forces during the halide exchange process. Specifically, the S_N1-like mechanism is primarily propelled by spontaneous perovskite dissolution and recrystallization, while the S_N2-like mechanism exhibits a clear temperature-dependent characteristic. Direct evidence is provided by in-situ halide exchange at low temperatures through using liquid nitrogen-cooled BACl-incorporated CF solution and perovskite substrates. As shown in Fig. 2d and Supplementary Fig. 11, the CF-based post-treatment fails to trigger effective halide exchange at low temperature, resulting in similar sky-blue emission at 488 nm to that of pristine film. Conversely, the same post-treatment at room temperature leads to apparently blue-shifted emission at 464 nm, highlighting the significant role of temperature for the CF-based halide exchange. Differently, the IPA-based post-treatment with the same BACl concentration yields blue-shifted emission at 453 and 470 nm at room and low temperatures, respectively. It is noteworthy that the change in solubility with temperature limits the spontaneous perovskite dissolution process in SN1-like mechanisms at low temperatures, which leads to different PL spectra of IPA post-treated films at room and low temperatures. Nevertheless, this temperature dependence has limited influence and the IPA post-treated film still exhibits a significant blue-shifted PL spectrum at low temperature.

These findings are supported by theoretical simulations, as depicted in the potential energy profiles of the halide exchange reaction (Fig. 2e), and the corresponding structures are summarized in Supplementary Fig. 12. The reaction enthalpy change for Cl replacing Br during halide exchange is −0.14 eV, indicating that the S_N1-and

https://doi.org/10.1038/s41467-024-55074-4

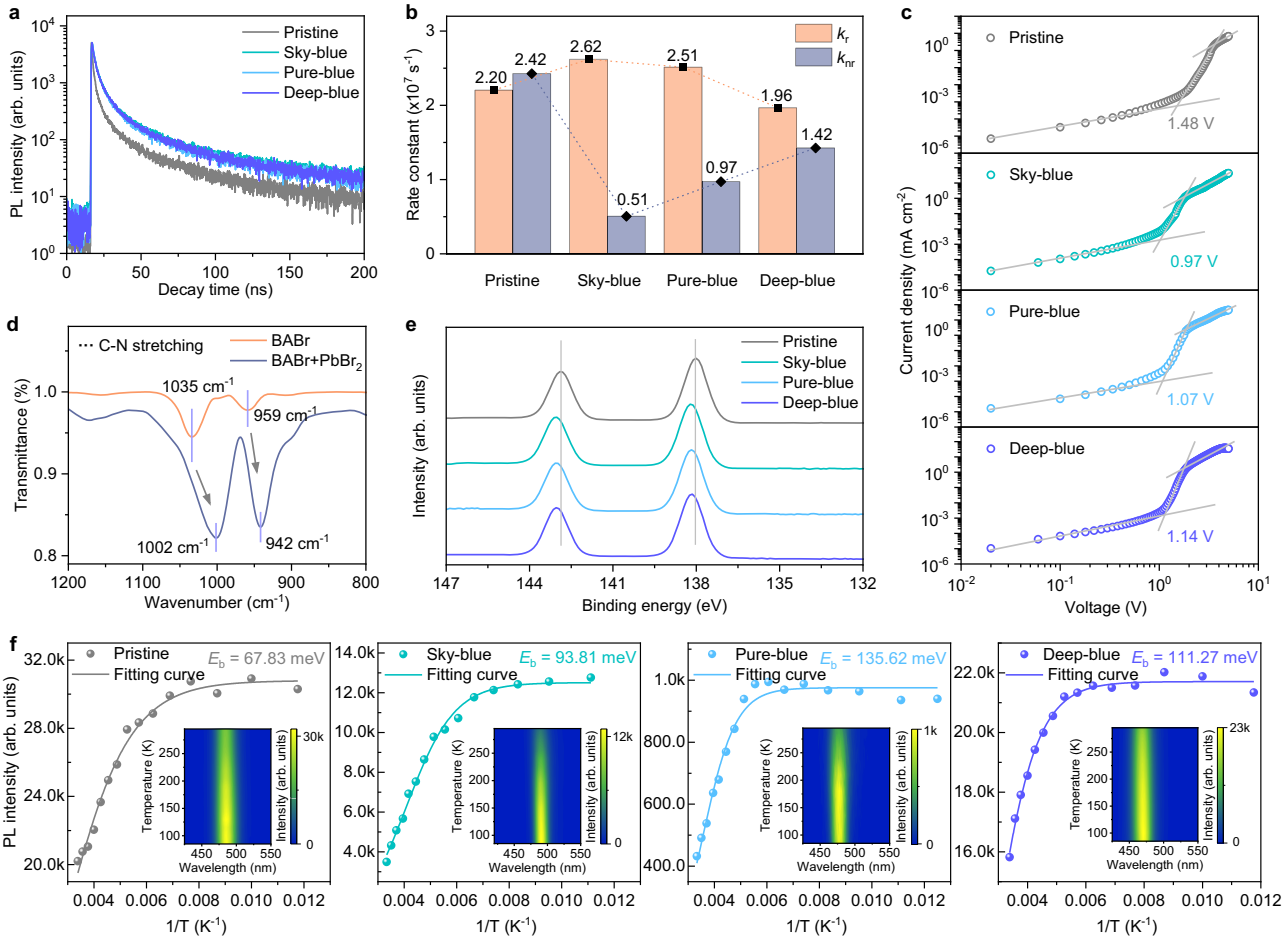

Fig. 3 | Photophysical properties of blue perovskite films. a TRPL spectra of pristine and post-treated perovskite films. **b** Recombination rates derived from TRPL and PLQY results. **c** *J-V* curves of hole-only devices in SCLC measurements. **d** FTIR spectra of pure BABr and BABr/$PbBr_2$ mixture. **e** XPS spectra of Pb *4f* core levels. **f** Relevant integration of the temperature-dependent PL intensity of perovskite films and fitting curves for E_b. Inset is the corresponding temperature-dependent PL spectra.

S_N2-like mechanisms are both thermodynamically feasible spontaneous processes. For the S_N1-like mechanism, an intermediate M1 with a defect formation energy of −0.18 eV is initially generated. Considering the entropy-increasing process of halogen dissolution in IPA, the spontaneous formation of halogen vacancies can be inferred. To complete halogen ion exchange, the intermediate M1 needs to overcome a barrier of 0.04 eV, which might be the main reason for the limited bandgap regulation by IPA-based post-treatment at low temperature. In comparison, the S_N2-like mechanism starts with a high activation energy 1.02 eV to form the intermediate M2, corresponding to the surface adsorption of Cl atoms. Then, the formation of the transition state TS1 requires a barrier of 0.32 eV, necessitating suitable temperature to initiate the halide exchange process, which aligns with the strong temperature dependence observed for the CF-based post-treatment. Additionally, unlike IPA-based post-treatment, BABr-incorporated CF solution does not induce a redshift spectrum at room temperature (Supplementary Fig. 13). Compared to the exchange process of substituting Cl for Br atoms, the substitution of Br for Cl atoms has a higher activation energy barrier (Supplementary Fig. 14), due to the increased ionic radius (from 1.81 Å of Cl to 1.96 Å of Br) and the reduced interstitial space (from 6.0 Å in $CsPbBr_3$ to 5.61 Å in $CsPbCl_3$) (Supplementary Fig. 12), which inhibits the halide exchange process at room temperature. Notably, upon heating the CF-based post-treatment solution and perovskite substrate, a redshift spectrum of perovskite film was observed (Supplementary Fig. 13), which further supports our theory.

Photophysical properties of the post-treated films

Leveraging the S_N2-like ionic exchange mechanism, the CF-based post-treatment imparts excellent photophysical properties to blue perovskite films via nondestructive bandgap modulation. By fixing the molar ratio of BABr to BACl in the CF at 7:3; 4:6, and 1:9, we achieved sky-, pure-, and deep-blue emissions and all subsequent research built upon these findings. We firstly investigated the exciton dynamics in perovskite films by TRPL measurements (Fig. 3a). All post-treated perovskite films exhibit similar decay curves, which can be attributed to the similar halide vacancy filling and passivation effect of BAX ligands at the same concentration (Supplementary Table 1). The τ_{avg} for the sky-, pure-, and deep-blue films are fitted to be 31.98, 27.68, and 29.48 ns, respectively, which are all higher than that of pristine film (21.58 ns), indicating the effective suppression of the trap-mediated nonradiative recombination loss[27,28]. Compared to the control perovskite film, the sky-, pure-, and deep-blue samples yield much improved PLQYs of 83.8%, 72.1%, and 58.0%, respectively (Supplementary Fig. 15). Notably, although all the post-treated perovskite films exhibit similar TRPL curves, the increased deep-level traps and reduced defect tolerance induced by higher Cl/Br ratio greatly degrade the PLQYs of the perovskite films with wider bandgaps. Furthermore, a quantitative analysis of the exciton dynamics was conducted by employing the following equations[29,30]: PLQY = $k_r/(k_r + k_{nr})$ and $\tau_{average} = 1/(k_r + k_{nr})$, where k_r and k_{nr} represent the radiative and nonradiative recombination constants (Supplementary Note 1), respectively. As shown in Fig. 3b, the target films exhibit much lower k_{nr}

https://doi.org/10.1038/s41467-024-55074-4

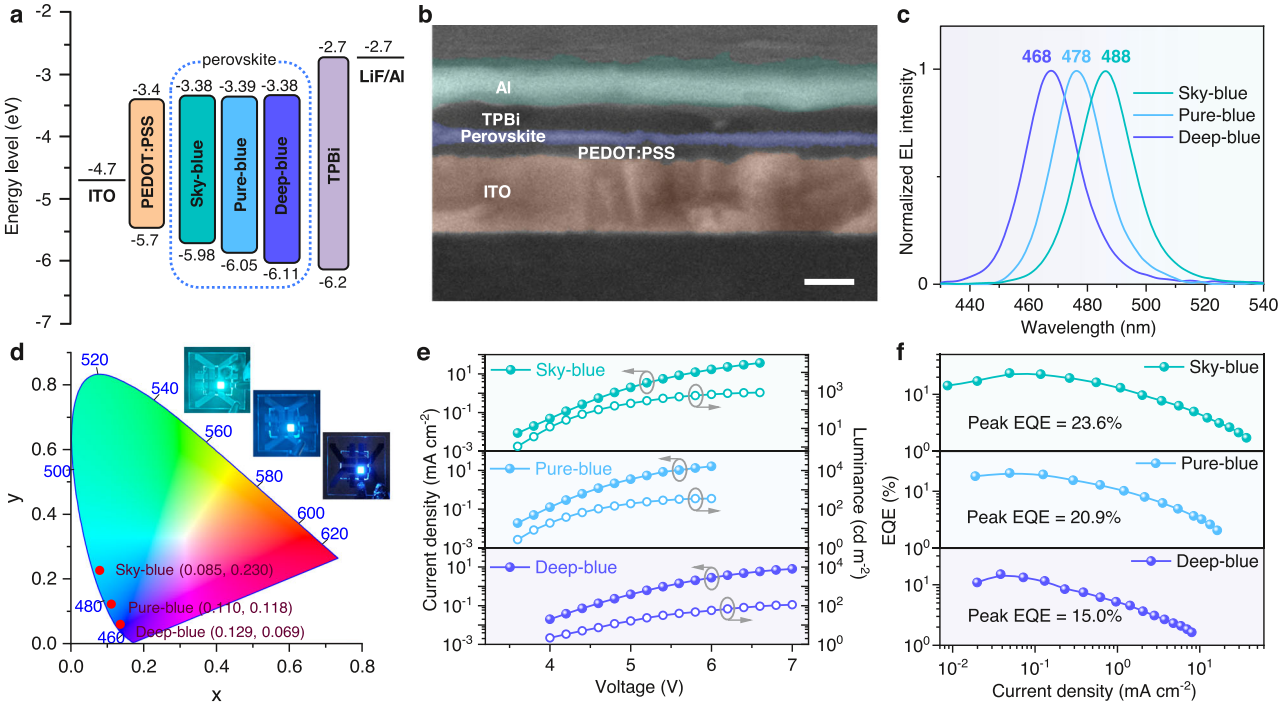

Fig. 4 | Device structure and performance of blue PeLEDs. a Energy levels of functional layers in sky-, pure- and deep-blue PeLEDs. **b** Device cross-sectional SEM image. Scale bar: 100 nm. **c** Normalized EL spectra. **d** CIE coordinates and photographs of blue PeLEDs. **e** *J-V-L* characteristics. **f** Dependence of the EQE versus current density.

values compared to the pristine sample, indicating reduced nonradiative energy loss. Meanwhile, the enlarged bandgap limits the exciton radiative recombination and hence results in a decrease in k_r. Due to the increased Cl content, the wide bandgap leads to a lower defect tolerance for perovskite films, which causes gradually increased k_{nr}. Since the CF-based post-treatment possesses similar defect passivation capability for perovskite films with different bandgaps, the possibility that trap density predominantly governs k_{nr} can be ruled out

To quantitatively evaluate the impact of CF-based post-treatment on the trap density of perovskite films, space-charge limited current (SCLC) method was used by constructing hole-only devices with the structure of ITO/PEDOT:PSS/perovskite/4,4′-N,N′-dicarbazole-biphenyl (CBP)/molybdenum oxide (MoO_x)/Ag. As shown in Fig. 3c, the dark current density-voltage (*J-V*) curves of hole-only devices exhibit significant changes in the trap-fill-limited regions. The initial trap-fill-limited voltage (V_{TFL}) decreases from 1.48 V of the pristine device to 0.97 V (sky-blue), 1.07 V (pure-blue), and 1.14 V (deep-blue) in the post-treated devices, indicating the lower trap densities in the post-treated perovskite films. Further evidence is provided by the trap density (N_t) quantitative calculations[31], where the trap state densities for the pristine, sky-, pure-, and deep-blue perovskite films are estimated to be 3.99×10^{18}, 2.61×10^{18}, 2.88×10^{18}, and 3.07×10^{18} cm^{-3}, respectively. The significantly reduced trap densities benefit from the passivation effect of BA cations. To examine the chemical interaction between the perovskites and the BA ligands, we performed Fourier transform infrared spectroscopy (FTIR) measurements (Fig. 3d). Compared to the signals from pure BABr, the FTIR peaks corresponding to the C-N stretching vibrations are shifted to lower wavenumbers by mixing lead bromide ($PbBr_2$) with BABr sample, which indicates the weakening and lengthening of the C-N bond[32]. We ascribe this phenomenon to the coordination interaction between the amine groups (-NH_2) from BA cations and the undercoordinated Pb atoms in perovskites, contributing to conducive defect passivation for the target perovskite films. Furthermore, XPS measurements were conducted on perovskite films to confirm the interaction between Pb atoms and BA ligands. The CF-based post-treatment brings about a clear XPS spectral shift from the Pb 4*f* core level (Fig. 3e), providing further evidence for the strong interaction between perovskites and the BA cations[27].

To further investigate the passivation mechanism of the CF-based post-treatment, we conducted temperature-dependent PL measurements and the integrated PL intensity is summarized in Fig. 3f. The decreased PL intensity of perovskite films with increasing temperature results from the trap-assisted nonradiative thermal quenching. The exciton binding energies (E_b) in perovskite films were calculated through curve fitting (Supplementary Note 2). Compared to the pristine film with an E_b of 67.83 meV, the post-treated sky-, pure-, and deep-blue films feature significantly improved E_b of 93.81, 135.62, and 111.27 meV, respectively. The boost in E_b reduces the probability of excitons dissociating into free carriers, thereby suppressing defect-mediated free carrier trapping and enhancing radiative recombination[23,33,34]. Furthermore, the scanning electron microscopy (SEM) images demonstrate that the CF-based post-treatment not only enables smooth and dense perovskite films, but also effectively eliminates the incomplete crystallization of white $PbBr_2$ particles as displayed on the pristine film surface (Supplementary Fig. 16)[35]. The morphological evolution of perovskite films matches well with the GIWAXS results as shown in Supplementary Fig. 9. The CF-based post-treatment distinctly attenuates the scattering rings (at 9 nm^{-1}) related to the precursor $PbBr_2$ particles on perovskite films. The elimination of surface excess $PbBr_2$ benefits to constructing high-quality perovskite films with uniform film morphology and minimized interfacial charge loss[36].

Efficient blue PeLEDs by nondestructive halide exchange

Encouraged by the tunable bandgaps and low defect densities of the target blue perovskite films, we fabricated PeLEDs with sky-, pure-, and deep-blue emission to assess the impact of the nondestructive halide exchange strategy on device EL performance. Blue PeLEDs with the structure of ITO (150 nm)/PEDOT:PSS (30 nm)/Perovskite (20 nm)/TPBi (45 nm)/LiF (1 nm)/Al (80 nm). The device energy level diagram is schematically depicted in Fig. 4a, where the valence and conduction

bands of perovskite films were characterized through ultraviolet photoelectron spectroscopy (UPS) and Tauc plot analysis of the absorption spectra (Supplementary Figs. 17,18). The energy levels of PEDOT:PSS layers with varying ETA doping ratios were determined by the UPS spectra in Supplementary Figs. 19, 20, indicating that ETA modification facilitates the hole transport by reducing the energy barrier from PEDOT:PSS to perovskite films. The device structure was verified by the cross-sectional SEM image as displayed in Fig. 4b. Consistent with the PL results, by adjusting the molar ratio of Br:Cl in BAX, the target PeLEDs with tunable bandgaps exhibit sky-, pure-, and deep-blue EL emission at 488, 478, and 468 nm, respectively (Fig. 4c). Additionally, the corresponding Commission Internationale de l′ Eclairage (CIE) coordinates for these devices are (0.085, 0.230), (0.110, 0.118), and (0.129, 0.069), respectively (Fig. 4d). Notably, the EL emission from deep-blue device matches well with the NTSC standard, which showcases the great potential of CF-based halide exchange strategy towards new-generation displays. Figure 4e collects the current density-voltage-luminance (*J-V-L*) curves of blue PeLEDs. Compared to pristine device, the target devices exhibit slightly higher turn-on voltages due to the influence of BA ligand on charge injection. Benefitting from the nondestructive halide exchange via S_N2-like mechanism, the target devices achieve impressive EQE_{max} of 23.6%, 20.9%, and 15.0% with emission peaks at 488, 478, and 468 nm (Fig. 4f), respectively. To the best of our knowledge, our results represent the highest efficiencies recorded for sky-, pure-, and deep-blue PeLEDs (Supplementary Fig. 21), demonstrating the great potential of our strategy in producing highly efficient blue PeLEDs. It's noteworthy that the high EQEs of these blue PeLEDs rely on the good horizontal dipole orientation of the perovskite films. By fitting the angle-dependent PL test data, the horizontal transition dipole moments (TDMs) Θ of sky-, pure-, and deep-blue perovskite films reaches 83%, 84%, and 82%, respectively, which is higher than those of ideally isotropic emitters (67%) (Supplementary Fig. 22). A higher Θ is favorable for light extraction from the internal perovskite films to air. Compared to 86% of the pristine film, the similar Θ values in the post-treated films support the reliability of the proposed non-destructive post-treatment strategy. Moreover, the small thicknesses of perovskite films may suppress the waveguide light loss within devices, further boosting the device light out-coupling. Additionally, the sky-, pure-, and deep-blue PeLEDs exhibit good reproducibility with average peak EQEs of 11.95%, 17.76%, and 20.43%, respectively (Supplementary Fig. 23). In comparison, the sky-, pure-, and deep-blue PeLEDs with IPA-based halide exchange exhibit much inferior EQE_{max} of only 1.36%, 1.48%, and 0.83%, respectively (Supplementary Fig. 24). Compared to the pure-IPA post-treated devices, the slight efficiency improvement is on account of the halogen vacancy filling via S_N1-like mechanism. These distinct discrepancies by employing different halide exchange strategies indicate the great significance of nondestructive post-treatment for constructing high-performance blue PeLEDs.

To evaluate the EL stability of blue PeLEDs, the operational half-lifetime (T_{50}) was first measured under a constant current of 1 mA cm^{-2}. As shown in Supplementary Fig. 25, the T_{50} for the sky-, pure-, and deep-blue devices are estimated to be 346, 332, and 253 s, respectively, which showcases significant improvement compared to that of the pristine device (145 s). Additionally, the CF post-treated PeLEDs exhibit good spectral stability as evidenced by the slight EL spectral shift with increasing driven voltages, which is in accordance with their stable CIE coordinates (Supplementary Figs. 26, 27). In addition, the CF post-treated devices exhibit prolonged transient EL lifetimes following electric pulse stimulation, which is consistent with the TRPL results, further validating the effectiveness of the proposed strategy in reducing defect-induced trap state for mixed-halide blue perovskites (Supplementary Fig. 28)[37].

Apart from IPA and CF solvents, the S_N1-like and S_N2-like halide exchange mechanisms were validated by further expanding the solvent choices. The devices based on the post-treatment with other antisolvents, such as chlorobenzene (CB), toluene (Tol), and xylene (Xyl), also exhibited significantly improved device performance, as shown in Supplementary Figs. 29, 30. This is attributed to the protective effect of these antisolvents on perovskite films. Similar to IPA, solvents such as ethanol (EtOH) and butanol (BuOH) feature the similar erosive effect on perovskite films, leading to distinctly degraded luminescence efficiency and EL spectral stability, as shown in Supplementary Figs. 31–34. In conclusion, by exploring the interaction between post-treatment solvents and perovskites, the solvent range can be further expanded for achieving desirable luminescent properties from perovskites.

Discussion

In summary, we have demonstrated a nondestructive halide exchange strategy through anti-solvent post-treatment for blue perovskites. In this strategy, the anti-solvent CF post-treatment avoids the formation of new halogen vacancies and the BAX salts with long alkyl chains enables effective halogen ion exchange for tuning bandgap from sky- to deep-blue region. To unveil the underlying mechanism of halide exchange, we establish S_N1- and S_N2-like ion exchange models for IPA- and CF-based post-treatment, respectively. The BAX-incorporated CF post-treatment protects perovskite films from solvent erosion and induces Cl atom attacking Pb atom accompanied by Br desorption. The resultant blue PeLEDs exhibit impressive EQE_{max} of 23.6%, 20.9%, and 15.0% with spectrally stable emission at 488, 478, and 468 nm, respectively. This work provides insight into the microscopic halogen ion exchange process and develops a universal bandgap modulation strategy to further unlock the potential of mixed-halide blue PeLEDs.

Methods

Materials

Lead bromide ($PbBr_2$, 99.0%), cesium bromide (CsBr, 99.0%), and lead chloride ($PbCl_2$, 99.0%) were sourced from TCI. Potassium bromide (KBr, 99.5%) and chloroform (CF) were obtained from Alfa Aesar, while 4-fluorophenylethylammonium bromide (*p*-F-PEABr, 99.5%) was supplied by Xian Yuri Solar Co., Ltd. Butylammonium chloride (BACl), butylammonium bromide (BABr), and formamidine bromide (FABr) were acquired from Advanced Election Technology Co., Ltd. Dimethyl sulfoxide (DMSO), lithium fluoride (LiF, 99.99%), and molybdenum oxide (MoO_x) were procured from MACKLIN. Ethanolamine (ETA), identified by product number N281001, was purchased from Thermo Scientific. PEDOT:PSS (Clevios Al 4083) was supplied by Heraeus. Additionally, 4,4′N,N′-dicarbazole-biphenyl (CBP) and 1,3,5-Tris (1-phenyl-1H-benzimidazol-2-yl)benzene (TPBi) were obtained from Nichem. All chemicals were used as received without further purification.

Perovskite film preparation and device fabrication

The pristine perovskite precursor solution was prepared by dissolving $PbBr_2$ (0.037 M), $PbCl_2$ (0.062 M), CsBr (0.141 M), *p*-F-PEABr (0.049 M), FABr (0.016 M), and KBr (0.025 M) in DMSO, with the solution stirred for 12 hours at 40 °C. For the CF post-treatment, solutions of $BABr_{0.7}Cl_{0.3}$ (0.004 M), $BABr_{0.4}Cl_{0.6}$ (0.004 M), and $BABr_{0.1}Cl_{0.9}$ (0.004 M) were prepared by dissolving them in CF at room temperature for 2 hours, enabling the fabrication of sky-, pure-, and deep-blue perovskite films, respectively. The blue PeLEDs employed a layered structure consisting of ITO (150 nm)/PEDOT:PSS (30 nm)/Perovskite (20 nm)/TPBi (45 nm)/LiF (1 nm)/Al (100 nm). Patterned ITO glass substrates were cleaned sequentially by ultrasonication in detergent solution, deionized water, ethanol, and isopropanol for 7 minutes each, followed by drying in an oven at 90 °C for 120 minutes. Prior to PEDOT:PSS deposition, the ITO substrates underwent UV-ozone treatment (Novascan PSD Pro system) for 20 minutes at room temperature. Aqueous PEDOT:PSS was mixed with 4 vol.‰ ETA, stirred at

room temperature for 15 minutes, and stored at 2-5 °C. The modified PEDOT:PSS layer was applied to ITO by spin-coating at 4000 rpm for 40 seconds, followed by thermal annealing at 140 °C for 15 minutes. Perovskite films were formed by spin-coating the precursor solution onto the PEDOT:PSS layer at 4000 rpm for 60 seconds, with subsequent annealing at 70 °C for 5 minutes. Post-treatment was performed by spin-coating 60 uL of the CF solution onto the perovskite film at 5500 rpm for 50 seconds, without further annealing. After the preparation of the perovskite films, TPBi, LiF, and Al electrodes were sequentially deposited using thermal evaporation under a pressure below 2×10^{-6} Torr. The deposition rates and layer thicknesses were monitored with a quartz crystal microbalance. TPBi was deposited at 2 Å s^{-1} to a thickness of 40 nm, LiF at 0.1 Å s^{-1} to 1 nm, and Al at 5 Å s^{-1} to 100 nm. The active emitting area of the PeLEDs was 0.1 cm^2, defined by the overlap between the ITO and Al electrodes. Hole-only devices were fabricated with the architecture ITO/PEDOT:PSS/perovskite/CBP/MoO_x/Al.

Film and device characterizations

The morphology of blue perovskite films was analyzed using scanning electron microscopy (SEM, Zeiss G500). Steady-state photoluminescence (PL) spectra were recorded in an ambient environment with a FluoroMax-4 fluorescence spectrometer (Horiba Jobin Yvon). Transient PL decay was measured at room temperature using a Quantaurus-Tau fluorescence lifetime spectrometer (C11367-32, Hamamatsu Photonics) equipped with a pulsed laser operating at 373 nm, with a pulse width of 100 ps and a repetition rate of 5 kHz. The absorption spectra of sky-blue perovskite films were obtained using a Perkin Elmer Lambda 950 UV/Vis/NIR spectrometer. Absolute photoluminescence quantum yields (PLQYs) of blue perovskite films deposited on PEDOT:PSS substrates were determined at room temperature under nitrogen using a C9920-02G fluorescence spectrophotometer (Hamamatsu, Japan) with an integrating sphere and excitation wavelength of 365 nm. The excitation light intensity was approximately 6.0×10^7 (arbitrary units). Synchrotron-based Grazing-Incidence Wide-Angle X-ray Scattering (GIWAXS) experiments were conducted at the BL14B1 beamline of the Shanghai Synchrotron Radiation Facility using X-rays with a wavelength of 1.24 Å and a grazing incidence angle of 0.2°. The signal was collected by a Pilatus3s 2 M detector positioned ~286 mm from the sample, with an exposure time of 100 s. Two-dimensional X-ray diffraction (XRD) patterns, displayed in scattering q coordinates, were processed using FIT2D software. X-ray photoelectron spectroscopy (XPS) was performed using an ultrahigh vacuum photoemission spectroscopy system (Kratos AXIS UltraDLD) with a monochromatic Al Kα source (1486.6 eV). Ultraviolet photoelectron spectroscopy (UPS) measurements employed unfiltered He I radiation (21.22 eV) from a discharge lamp with a total energy resolution of 100 meV. The current density-voltage-luminance (*J-V-L*) characteristics and electroluminescence (EL) spectra of PeLEDs were simultaneously measured in ambient air at room temperature using a Hamamatsu Photonics C9920-12 integrating sphere. These results were verified using a programmable power source (Keithley model 2400) and a luminance meter/spectrometer (Photo Research PR670).

Computational details

Density functional theory (DFT) calculations were carried out using the projector augmented plane-wave method implemented in the Vienna Ab initio Simulation Package (VASP)[38,39]. The exchange-correlation functional was described using the Perdew-Burke-Ernzerhof (PBE) formulation within the generalized gradient approximation (GGA)[40]. A plane-wave energy cutoff of 450 eV was applied, and the iterative solution of the Kohn-Sham equations used an energy convergence criterion of 10^{-5} eV. Structural relaxation was performed until the residual atomic forces were reduced below 0.02 eV $Å^{-1}$. To eliminate interactions between periodic images along the vertical axis, a vacuum layer of 15 Å was introduced. A Monkhorst-Pack k-point grid of $1 \times 1 \times 1$ was employed. The climbing-image nudged elastic band (CI-NEB) method was utilized to investigate the diffusion barriers of hydrogen at various adsorption sites.

Data availability

The data that support the findings of this study are provided in the Source Data file. Source data are provided with this paper.

References

1. Liu, X.-K. et al. Metal halide perovskites for light-emitting diodes. *Nat. Mater.* **20**, 10–21 (2021).
2. Zhang, K. et al. Blue halide perovskite materials: preparation, progress, and challenges. *Laser Photonics Rev.* **17**, 2200689 (2023).
3. Cao, Y.-B. et al. High-efficiency, flexible and large-area red/green/blue all-inorganic metal halide perovskite quantum wires-based light-emitting diodes. *Nat. Commun.* **14**, 4611 (2023).
4. Nong Y. et al. Boosting external quantum efficiency of blue perovskite QLEDs exceeding 23% by trifluoroacetate passivation and mixed hole transportation design. *Adv. Mater.* **36**, 2402325 (2024).
5. Yuan S. et al. Efficient blue electroluminescence from reduced-dimensional perovskites. *Nat. Photon.* **18**, 1–7 (2024).
6. Tong, Y. et al. In situ halide exchange of cesium lead halide perovskites for blue light-emitting diodes. *Adv. Mater.* **35**, 2207111 (2023).
7. Xia, Y. et al. Vertically concentrated quantum wells enabling highly efficient deep-blue perovskite light-emitting diodes. *Angew. Chem. Int. Ed.* **63**, e202403739 (2024).
8. Xing, J. et al. Color-stable highly luminescent sky-blue perovskite light-emitting diodes. *Nat. Commun.* **9**, 3541 (2018).
9. Gong, X. et al. Electron–phonon interaction in efficient perovskite blue emitters. *Nat. Mater.* **17**, 550–556 (2018).
10. Wang, C. et al. Dimension control of in situ fabricated $CsPbClBr_2$ nanocrystal films toward efficient blue light-emitting diodes. *Nat. Commun.* **11**, 6428 (2020).
11. Alahbakhshi, M. et al. Highly efficient quasi 2D blue perovskite electroluminescence leveraging a dual ligand composition. *Adv. Funct. Mater.* **33**, 2214315 (2023).
12. Jia, Y. et al. Unveiling the complex evolution in mixed Br-Cl perovskite precursors for high-efficiency deep-blue light-emitting diodes. *Small Struct.* **4**, 2200393 (2023).
13. Li, G. et al. Highly efficient perovskite nanocrystal light-emitting diodes enabled by a universal crosslinking method. *Adv. Mater.* **28**, 3528–3534 (2016).
14. Shen, K.-C. et al. Unraveling the role of crystallization dynamics on luminescence characteristics of perovskite light-emitting diodes. *Laser Photonics Rev.* **15**, 2100023 (2021).
15. Jiang, N. et al. 2D/3D Heterojunction perovskite light-emitting diodes with tunable ultrapure blue emissions. *Nano Energy* **97**, 107181 (2022).
16. Zhao, S. et al. Postdeposition halide exchange for achieving deep-blue perovskite light-emitting diodes: the role of the organic cations in the chloride source. *Small Methods* **8**, 2300572 (2024).
17. Yoon, Y.-J. et al. Highly stable bulk perovskite for blue LEDs with anion-exchange method. *Nano Lett.* **21**, 3473–3479 (2021).
18. Zhao, T. et al. Realization of a highly oriented $MAPbBr_3$ perovskite thin film via ion exchange for ultrahigh color purity green light emission. *ACS Energy Lett.* **3**, 1662–1669 (2018).
19. Xiao, S. et al. Post-treatment techniques for high-performance perovskite solar cells. *Mrs Bull.* **45**, 431–438 (2020).
20. Zeng, M. et al. Deep-blue perovskite light-emitting diodes realized by a dynamic interfacial ion exchange. *ACS Appl. Mater. Interfaces* **15**, 36620–36627 (2023).

21. Jiang, K. et al. Alkyl chain tuning of small molecule acceptors for efficient organic solar cells. *Joule* **3**, 3020–3033 (2019).
22. Li, C. et al. Non-fullerene acceptors with branched side chains and improved molecular packing to exceed 18% efficiency in organic solar cells. *Nat. Energy* **6**, 605–613 (2021).
23. Zhang, K. et al. Top-down exfoliation process constructing 2d/3d heterojunction toward ultrapure blue perovskite light-emitting diodes. *ACS nano* **18**, 4570–4578 (2024).
24. Kumawat, N. K. et al. Structural, optical, and electronic properties of wide bandgap perovskites: experimental and theoretical investigations. *J. Phys. Chem. A* **120**, 3917–3923 (2016).
25. Peters, K. S. et al. Nature of dynamic processes associated with the S_N1 reaction mechanism. *Chem. Rev.* **107**, 859–873 (2007).
26. Hamlin, T. A. et al. Nucleophilic substitution (S_N2): dependence on nucleophile, leaving group, central atom, substituents, and solvent. *ChemPhysChem* **19**, 1315–1330 (2018).
27. Zhou, W. et al. Manipulating ionic behavior with bifunctional additives for efficient sky-blue perovskite light-emitting diodes. *Adv. Funct. Mater.* **33**, 2301425 (2023).
28. Shen, Y. et al. Interfacial nucleation seeding for electroluminescent manipulation in blue perovskite light-emitting diodes. *Adv. Funct. Mater.* **31**, 2103870 (2021).
29. Wang, B. et al. Low-dimensional phase regulation to restrain non-radiative recombination for sky-blue perovskite LEDs with EQE exceeding 15%. *Angew. Chem. Int. Ed.* **62**, e202219255 (2023).
30. Wang, J. et al. Increasing donor-acceptor spacing for reduced voltage loss in organic solar cells. *Nat. Commun.* **12**, 6679 (2021).
31. Jiang, Q. et al. Enhanced electron extraction using SnO_2 for high-efficiency planar-structure HC $(NH_2)_2PbI_3$-based perovskite solar cells. *Nat. Energy* **2**, 1–7 (2016).
32. Wang, M. et al. A universal strategy of intermolecular exchange to stabilize α-$FAPbI_3$ and manage crystal orientation for high-performance humid-air-processed perovskite solar cells. *Adv. Mater.* **34**, 2200041 (2022).
33. Zhu, H. et al. Enriched-bromine surface state for stable sky-blue spectrum perovskite QLEDs with an EQE of 14.6%. *Adv. Mater.* **34**, 2205092 (2022).
34. Wang, H. et al. Molecule-induced p-doping in perovskite nanocrystals enables efficient color-saturated red light-emitting diodes. *Small* **16**, 2001062 (2020).
35. Wang, J. et al. Growth and degradation kinetics of organic–inorganic hybrid perovskite films determined by in situ grazing-incidence X-ray scattering techniques. *Small Methods* **5**, 2100829 (2021).
36. Shen, Y. et al. Interfacial "anchoring effect" enables efficient large-area sky-blue perovskite light-emitting diodes. *Adv. Sci.* **8**, 2102213 (2021).
37. Shen, Y. et al. Interfacial potassium-guided grain growth for efficient deep-blue perovskite light-emitting diodes. *Adv. Funct. Mater.* **31**, 2006736 (2021).
38. Kresse, G. et al. Ab initio molecular-dynamics simulation of the liquid-metal–amorphous-semiconductor transition in germanium. *Phys. Rev. B* **49**, 14251 (1994).
39. Kresse, G. et al. Efficient iterative schemes for ab initio total-energy calculations using a plane-wave basis set. *Phys. Rev. B* **54**, 11169 (1996).
40. Perdew, J. P. et al. Accurate and simple analytic representation of the electron-gas correlation energy. *Phy. Rev. B* **45**, 13244 (1992).

Acknowledgements

J.T. acknowledges financial support from the National Key R&D Program of China (No. 2022YFE0108900), the National Natural Science Foundation of China (Nos. 62320106004, 62274117), the Science and Technology Development Fund (FDCT), Macao SAR (No. 0018/2022/A1), and Collaborative Innovation Center of Suzhou Nano Science & Technology. Y.L. acknowledges the Science and Technology Innovation Plan of Shanghai Science and Technology Commission (No. 22520760600) and the National Natural Science Foundation of China (No. 62075061). Y.S. acknowledges the National Natural Science Foundation of China (Nos. 62405208).

Author contributions

K.Z., Y.S., and J.T. conceived the idea for the study and designed the experiments. L.C. prepared the perovskite precursors and films. K.Z. fabricated the devices and carried out the DFT calculations. X.H. and S.F. performed the film characterizations. H.L. and F.X. assisted in film characterizations and data analysis. Z.S. and X.G. carried out grazing-incidence wide-angle X-ray scattering the measurement. B.W. carried out femtosecond transient absorption measurement. K.Z. and Y.S. analyzed the data and wrote the manuscript. Y.L. and J.T. edited the manuscript. All authors contributed to the manuscript.

Competing interests

The authors declare no competing interests.

Additional information

Supplementary information The online version contains supplementary material available at https://doi.org/10.1038/s41467-024-55074-4.

Correspondence and requests for materials should be addressed to Yang Shen, Yan-Qing Li or Jian-Xin Tang.

Peer review information *Nature Communications* thanks Gi-Hwan Kim and the other anonymous reviewer(s) for their contribution to the peer review of this work. A peer review file is available.